Journal of The
Electrochemical Society



# Key Role of Magnetite in Rust Layer of Carbon Steel for Cathodic Reactions and Hydrogen Permeation

*Journal of The Electrochemical Society*, 2026 **173** 091502

# Key Role of Magnetite in Rust Layer of Carbon Steel for Cathodic Reactions and Hydrogen Permeation

**Mariko Kadowaki,*,z Masahiro Yamamoto, Hideki Katayama,* Arkapol Saengdeejing, Taichi Abe, Ryoji Sahara, Kotaro Doi, Yoshiharu Murase, Sachiko Hiromoto, and Yusuke Tsutsumi***

*National Institute for Materials Science, Tsukuba 305-0047, Japan*

This study investigates the influence of rust layer composition on cathodic reactions and hydrogen permeation behavior of SM490 carbon steel exposed to NaCl-containing environments. Rust layers were formed on the SM490 specimens by repeated wet/dry cycles using NaCl-containing droplets. Polarization measurements revealed that rust formation and growth enhanced the cathodic reaction. The reduction reaction of rust components, particularly FeOOH, was identified as one of the predominant contributors to this enhancement. Notably, the results indicated that, in addition to the reduction of rust components, the hydrogen evolution reaction could actively proceed on $Fe_3O_4$. Because hydrogen evolution occurs less readily on FeOOH, an increase in the $Fe_3O_4$ fraction within the rust layer should promote hydrogen evolution reactivity and consequently enhance hydrogen permeation. This correlation was confirmed by electrochemical hydrogen permeation tests. These findings provided new insights into the relationship between rust layer composition and hydrogen permeation behavior, thereby advancing mechanistic understanding of hydrogen entry processes in practical steels under atmospheric corrosion conditions.
 [DOI: 10.1149/1945-7111/ae6483]

Manuscript submitted March 12, 2026; revised manuscript received April 16, 2026. Published May 6, 2026.

High-strength steels are extensively utilized as structural materials in automobiles and transportation systems owing to their excellent mechanical properties. However, hydrogen embrittlement remains a critical problem that significantly limits structural reliability by causing a reduction in ductility and localized brittle fracture. In recent years, intensive research efforts have been devoted to elucidating the mechanisms governing hydrogen permeation and embrittlement in steels.[1–3]

Structural steels are frequently exposed to atmospheric environments, where the formation of rust layers on their surfaces is inevitable. The presence of rust and corrosion products is known to significantly influence the susceptibility of steels to hydrogen permeation.[4–11] Zakroczymski et al. reported that long, uninterrupted cathodic polarization of iron in 0.1 M NaOH resulted in the metal surface becoming more prone to both hydrogen absorption and corrosion, and that this treatment leads to the formation of a corrosion product layer which does not hinder hydrogen absorption.[4] Sudha et al. conducted hydrogen charging on DP and IF steels in 0.1 M NaOH, and demonstrated that the effect of the rust layer depends on its structure; it can promote hydrogen uptake when it generates catalytic iron particles during reduction, but may also hinder hydrogen permeation by acting as a physical barrier.[11] While these findings were obtained in alkaline environments, there are also reports under conditions closer to atmospheric corrosion, such as NaCl solutions. For example, Akiyama et al. investigated hydrogen permeation behavior in boron-bearing and AISI 4135 steels during wet/dry cyclic corrosion tests using NaCl solutions and reported a strong correlation between rust formation and enhanced hydrogen permeation.[7] Similarly, Li et al. demonstrated that corrosion products formed on dispersion-strengthened-high-strength steel during seawater wet/dry cycles increased hydrogen permeation and embrittlement sensitivity, particularly in welded joints.[9] The promotion of hydrogen permeation by rust has been attributed to several factors, including local acidification beneath the rust layer[7,8,10] and restricted oxygen transport caused by rust coverage.[9]

Despite extensive research into the effect of rust layers on hydrogen permeation in alkaline and NaCl environments, the specific role of rust characteristics—including phase composition—has yet to be clearly understood. Under atmospheric corrosion conditions, rust layers generally consist of FeOOH ($\alpha$, $\gamma$, $\beta$, etc.) and $Fe_3O_4$.[12–17] However, the relative fraction of these components varies considerably depending on environmental conditions (temperature, relative humidity, atmospheric pollutants, etc.), steel composition, and corrosion morphology.[18,19] Clarifying how such compositional variations influence hydrogen permeation is essential for evaluating hydrogen embrittlement risk and improving the durability of structural steels in service environments.

Hydrogen permeation initiates through electrochemical hydrogen evolution reaction occurring on steel or rust layer surfaces. A fraction of the generated hydrogen by this reaction permeates into the steel and contributes to hydrogen embrittlement. Although various factors, such as steel surface adsorption characteristics and microstructure,[20–22] affect hydrogen permeation behavior, the hydrogen evolution reactivity is particularly one of the most critical factors governing the amount of hydrogen permeating into the steel.[23] Therefore, understanding the propensity for hydrogen evolution is essential for assessing the risk of hydrogen permeation and embrittlement.

The presence of rust is known to substantially alter the electrochemical behavior of steel.[24–30] Previous studies have discussed the influence of rust on anodic reactions on steel surfaces;[27,28] however, systematic understanding of cathodic reactions remains insufficient. In particular, information regarding the hydrogen evolution reactions on rust constituents is still scarce. Although rust layers composed of FeOOH ($\alpha$, $\gamma$, $\beta$, etc.) and $Fe_3O_4$ are commonly formed under atmospheric environments,[12–17] few researchers have quantitatively evaluated differences in hydrogen evolution activity between rusted and bare steel surfaces or identified the specific rust phase responsible for such differences.

The objective of this study was to investigate the influence of rust layer composition on cathodic reactions and hydrogen permeation behavior of SM490 carbon steel exposed to NaCl-containing environments. Rust layers were formed by repeating wet/dry cycles with NaCl-containing droplets, followed by polarization measurements. To isolate the effect of $Fe_3O_4$, a $Fe_3O_4$-dominant specimen was fabricated via spark plasma sintering and subjected to identical electrochemical evaluation. Based on these investigations, the role of $Fe_3O_4$ in promoting hydrogen evolution and associated hydrogen permeation was systematically examined using electrochemical hydrogen permeation tests.

## Experimental Methods

***SM490 specimens and wet/dry cycling.***—Commercial SM490 carbon steel sheets (thickness: 2 mm) were used in this study, and the

*Electrochemical Society Member.
zE-mail: KADOWAKI.Mariko@nims.go.jp

chemical composition is listed in Table I. For all experiments except hydrogen permeation tests, the sheets were cut into coupons measuring 15 mm × 15 mm. For hydrogen permeation tests, specimens with dimensions of 30 mm × 30 mm were prepared. Prior to experiments, specimen surfaces were mechanically polished using 1200-grit SiC paper followed by polishing with 1 μm diamond paste. Rust layers were subsequently formed by subjecting the specimens to repeated wet/dry cycles using NaCl-containing droplets, following the procedure reported our previous study.[31] The SM490 specimens were placed horizontally in a temperature- and humidity-controlled chamber maintained at 25 °C and 60% relative humidity. During the initial cycle, a 500 μl droplet containing 1 wt% NaCl was deposited onto the specimen surface. Under these conditions, the droplet completely dried within approximately 2.5 h, leaving NaCl residue on the surface. Subsequently, a 500 μl droplet of distilled water was added to re-form the NaCl-containing droplet. This wet/dry process was repeated for 5, 10, or 20 cycles.

***Preparation of $Fe_3O_4$ sintered specimen.***—A $Fe_3O_4$ specimen was fabricated by spark plasma sintering of commercially available $Fe_3O_4$ powder (Kanto Chemical Co., Inc., purity 95%). Sintering was performed using a LABOX-110 spark plasma sintering system (Sinter Land Inc.) under vacuum conditions of approximately 10 Pa. Although $Fe_3O_4$ is the main component in the commercial powder, minor impurities such as bcc Fe or $Fe_2O_3$ may be present due to phase transformations when the oxygen partial pressure during the powder manufacturing process deviates slightly from the exact equilibrium oxygen concentration of $Fe_3O_4$ (0.5714 at%).[32] If bcc Fe exists as an impurity in the commercial powder, heating to high temperature during sintering may induce phase transformation ($Fe+Fe_3O_4 \rightarrow 4FeO$), thereby reducing the $Fe_3O_4$ fraction in the obtained sintered specimen. Similarly, the presence of $Fe_2O_3$ may also promote phase transformation that decrease $Fe_3O_4$ fraction. To maximize the $Fe_3O_4$ fraction, it is necessary to perform sintering at temperatures at which such phase transformations cannot occur, even if these impurities are present in the commercial powder. Based on these considerations, the sintering temperature was determined based on the phase diagrams shown in Fig. 1.

Figure 1 shows the calculated temperature-pressure phase diagram from the thermodynamic assessment of the Fe–O binary system.[33] The equilibrium oxygen concentration of $Fe_3O_4$ is 0.5714 at%. In Fig. 1a, the oxygen concentration is slightly below the $Fe_3O_4$ equilibrium (0.571 at% O), where the two-phase region of bcc Fe and $Fe_3O_4$ at lower temperature. It corresponds to the case that bcc Fe coexists with $Fe_3O_4$ as an impurity in the powder. If such powder is used for sintering, at 10 Pa (sintering condition of this paper, indicated by a red dashed line in Fig. 1), the region where $Fe_3O_4$ and bcc Fe coexist stably extends up to 559 °C. This means that when bcc Fe is present as an impurity, phase transformation can be avoided below 559 °C at 10 Pa. In contrast, if it was heated above 559 °C, the phase transformation between Fe and $Fe_3O_4$ ($Fe+Fe_3O_4 \rightarrow 4FeO$) occurs, resulting in a decreased fraction of $Fe_3O_4$ in the obtained sintered specimen. Figure 1b shows the similar phase diagram where the oxygen concentration is slightly higher than the $Fe_3O_4$ equilibrium (0.572 at% O). This condition corresponds to the case where $Fe_2O_3$ coexists with $Fe_3O_4$ as an impurity. If this powder is used for sintering, at 10 Pa, $Fe_3O_4$ and $Fe_2O_3$ can coexist stably at temperatures up to 1105 °C. In other words, the phase transformation can be avoided below 1105 °C. It is preferable to perform sintering at the highest temperature to ensure sufficient densification, while preventing aforementioned phase transformations. Therefore, the sintering temperature in this study was determined to be 550 °C.

**Table I. Chemical compositions of SM490 (mass%).**

| C | Si | Mn | P | S | Fe |
|---|---|---|---|---|---|
| 0.15 | 0.20 | 0.84 | 0.02 | 0.05 | Bal. |

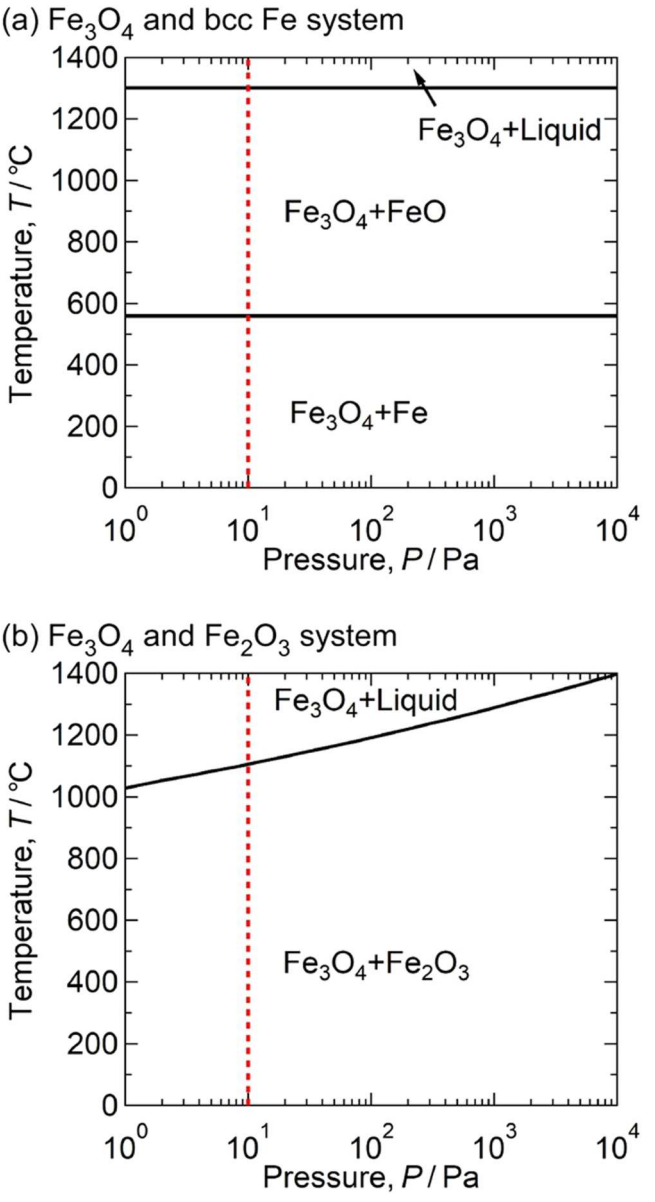


**Figure 1.** Calculated temperature-pressure phase diagrams from the thermodynamic assessment of the Fe-O binary system. (a) The oxygen concentration is set as 0.571 at%, corresponding to the case that bcc Fe coexists with $Fe_3O_4$ as an impurity in the powder. (b) The oxygen concentration is set as 0.572 at %, corresponding to the case that $Fe_2O_3$ coexists with $Fe_3O_4$ as an impurity in the powder.

The powder was loaded into a cylindrical graphite die with a diameter of 15 mm. Under an applied pressure of 5.3 kPa, the temperature was increased from room temperature to 550 °C over 30 min, and maintained at this temperature for 4 h. The specimen was subsequently cooled to room temperature.

***Polarization measurements.***—Potentiodynamic polarization measurements for the SM490 specimens (with and without rust layers) were conducted using a conventional three-electrode cell with a platinum counter electrode and an Ag/AgCl (3 M KCl) reference electrode. All potentials reported in this study are referenced to this electrode. The measurements were performed in naturally aerated 1 wt% NaCl solution at room temperature using an EC Frontier VM3 electrochemical cell. The SM490 specimen was positioned

horizontally, and the cell was sealed against the surface using an O-ring, providing an exposed area of 1 $cm^2$. Prior to polarization measurements, specimens were stabilized at the open circuit potential for 10 minutes. Potential scans were subsequently conducted at a scan rate of 20 mV $min^{-1}$, in accordance with our previous studies.[34–36]

Potentiostatic polarization measurements were also conducted for SM490 specimens (with and without rust layers) and the $Fe_3O_4$ specimen fabricated by spark plasma sintering. These measurements were carried out in 1 wt% NaCl solution at −1.0 V for 7 h, at room temperature under naturally aerated conditions. The cell configuration, including the counter and reference electrodes, was identical to that used for potentiodynamic measurements. For the SM490 specimens, the connection to the cell was performed in the same manner as described above for potentiodynamic polarization. For the $Fe_3O_4$ specimen, to prevent solution ingress into the specimen if surface pores were present, the specimen was suspended over the solution, exposing only the outermost surface to the solution. Prior to immersion, all areas of the $Fe_3O_4$ specimen except the outermost surface were coated with epoxy resin to prevent contact with the solution.

***X-ray diffraction analysis.***—X-ray diffraction (XRD) analysis was performed to determine the phase compositions of rust layers on the SM490 specimens before and after the potentiostatic polarization, and to characterize the sintered $Fe_3O_4$ specimen. Measurements were carried out using a BRUKER Advanced X-ray Solutions D2 Phaser with Cu-K$\alpha$ radiation, a step width of 0.02° and a scan rate of 1° $min^{-1}$.

***Microscopic observation.***—For the rust layers on the SM490 specimens, surface appearance before and after potentiostatic polarization measurements was examined using an optical digital microscope (KEYENCE, VHX 5000). Cross-sectional observations of rust layers were performed by a scanning electron microscope (SEM, HITACHI High-Tech SU5000) operated at an accelerating voltage of 15 kV. In addition, for the sintered $Fe_3O_4$ specimen, the surface appearance and topography were analyzed using a 3D microscope (KEYENCE, VR Series One-shot 3D).

***Hydrogen permeation test.***—Electrochemical hydrogen permeation tests were conducted using a Devanathan-Stachurski cell.[37,38] The SM490 specimen was positioned horizontally between the cathodic polarization cell (commonly referred to as hydrogen charging cell) and the detection cell, as illustrated in Fig. 2. The rusted surface served as the cathodic polarization side. The hydrogen detection side was coated with nickel plating. Nickel plating was carried out in an electrolyte containing $NiSO_4{\cdot}6H_2O$ (250 g $l^{-1}$), $NiCl_2{\cdot}6H_2O$ (45 g $l^{-1}$), and $H_3BO_3$ (40 g $l^{-1}$) at 60 °C under galvanostatic polarization at −3 mA $cm^{-2}$ for 180 s.

Two types of specimens with different rust compositions were prepared: (1) the specimen subjected to 10 wet/dry cycles with 1 wt% NaCl-containing droplets resulting in a FeOOH-dominant rust layer, and (2) the specimen subjected to additional potentiostatic polarization at −1.0 V for 2.5 h in 1 wt% NaCl solution after the 10 wet/dry cycles resulting in a $Fe_3O_4$-dominant rust layer. After rust formation, specimens were stored in air at room temperature for at least 24 h prior to Ni plating and the hydrogen permeation test. This exposure period allowed any hydrogen that may have permeated the steel during above rust formation processes to diffuse out; therefore, it did not affect the results of the hydrogen permeation test.

The hydrogen detection side was potentiostatically polarized at 0.14 V in 0.1 M NaOH solution. Although Hg/HgO was used as the reference electrode for the detection cell, all potentials reported in this paper were converted to and are presented relative to the Ag/AgCl reference electrode. After the background current reached a steady value below 0.07 μA $cm^{-2}$, a 1 wt% NaCl solution (adjusted to pH 3 with HCl) was introduced into the cathodic polarization cell. Previous studies have reported that the hydrogen permeation current in rusted steel is around 0.1 to 0.2 μA $cm^{-2}$.[39] In this study, we ensured that the background current was sufficiently lower than these values. To observe the hydrogen permeation behavior clearly, an acidic solution (pH 3) was used in this experiment. The cathodic polarization side (rusted surface) was potentiostatically polarized at −1.0 V. During the hydrogen permeation tests, the cathodic current, which reflects the hydrogen evolution reaction and other cathodic reactions, was measured on the cathodic polarization side. The anodic current, corresponding to the oxidation of permeated hydrogen, was measured on the detection side.

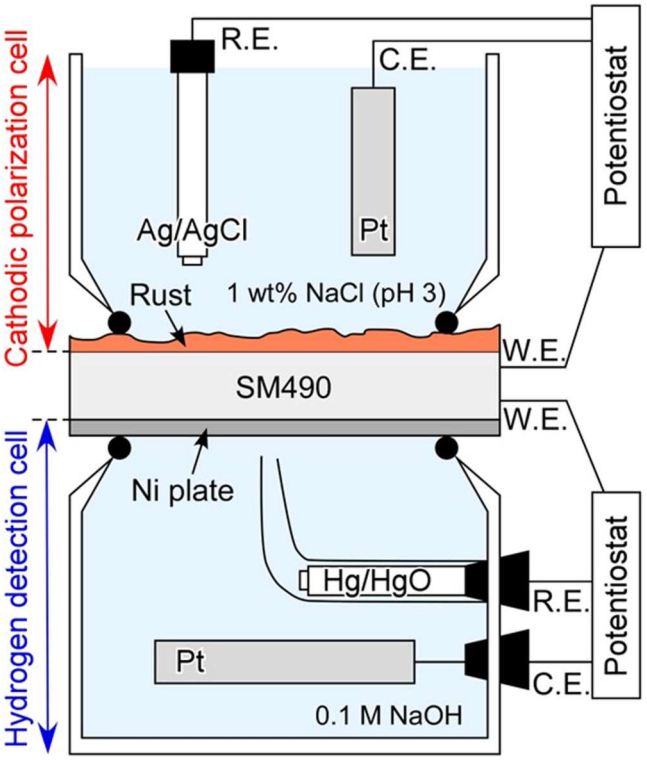


**Figure 2.** Schematic illustration of a Devanathan-Stachurski cell used for hydrogen permeation tests.

## Results and Discussion

***Characterization of rust layers formed during wet/dry cycles.***—Optical microscopy images of the SM490 specimen surfaces after 5, 10, and 20 wet/dry cycles using droplets containing 1 wt% NaCl are shown in Figs. 3a–3c. In all cases, the specimen surfaces were entirely covered with rust layers. The corresponding XRD patterns of these specimens are presented in Fig. 4. Diffraction peaks attributable to $\alpha$-FeOOH, $\gamma$-FeOOH, and $Fe_3O_4$ were observed for all specimens, indicating that the rust layers consisted primarily of these phases. Generally, FeOOH appears as red rust, whereas $Fe_3O_4$ exhibits a black coloration. Because the rust layers of all specimens exhibited reddish coloration in the optical images (Fig. 3), it is considered that FeOOH is the dominant constituent. The cross-sectional SEM images of the rust layers are shown in Fig. 5. The rust layer thickness increased progressively with increasing number of wet/dry cycles, confirming continuous rust growth during cyclic exposure.

As a side note, for the specimen after 5 cycles in Fig. 4, the Fe signal (around $2\theta = 44.5°$) was shifted toward the high-angle side, which is likely due to the influence of surface roughness. According to previous studies, surface roughness can affect XRD peak positions.[40] As the number of wet/dry cycles increases, the rust layer becomes more homogeneous, and this peak shift is no longer observed.

***Enhancement of the cathodic reaction by the presence of rust layer.***—To clarify changes in electrochemical behavior associated

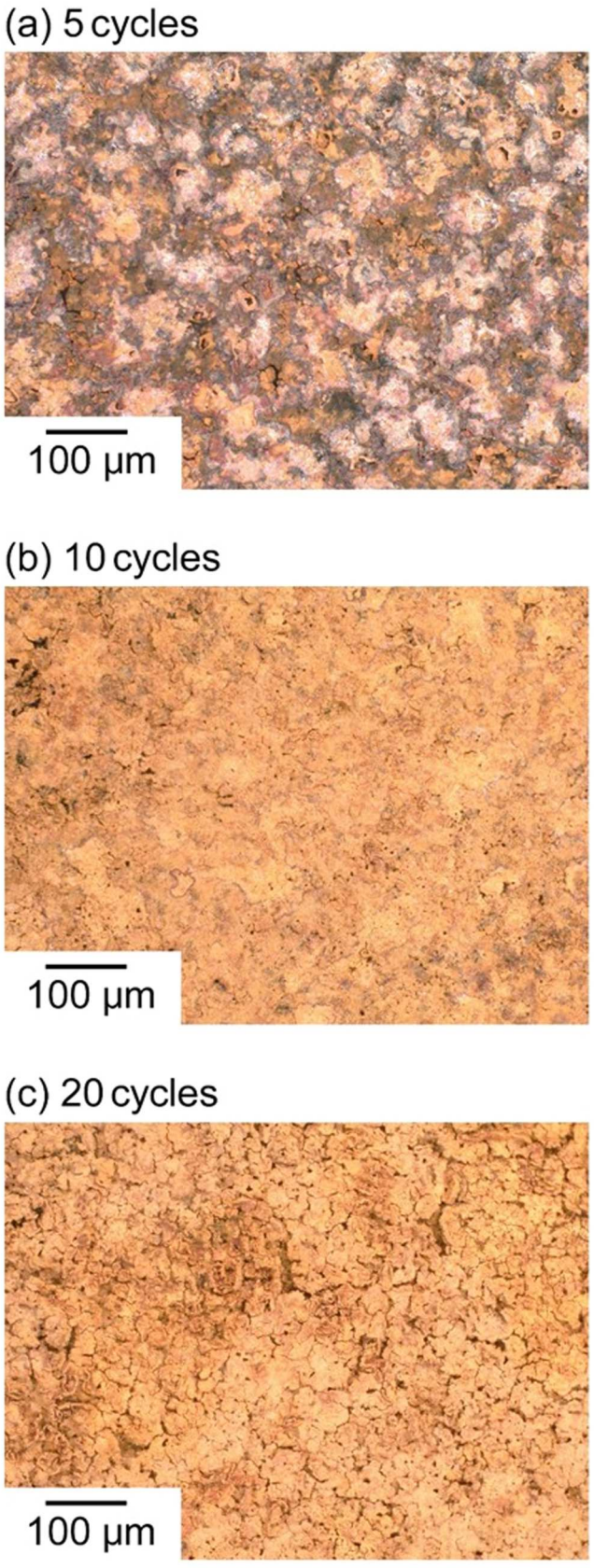


**Figure 3.** Optical microscopy images of rust layers formed on SM490 specimens after repeating wet/dry cycles: (a) after 5 cycles, (b) after 10 cycles, and (c) after 20 cycles.

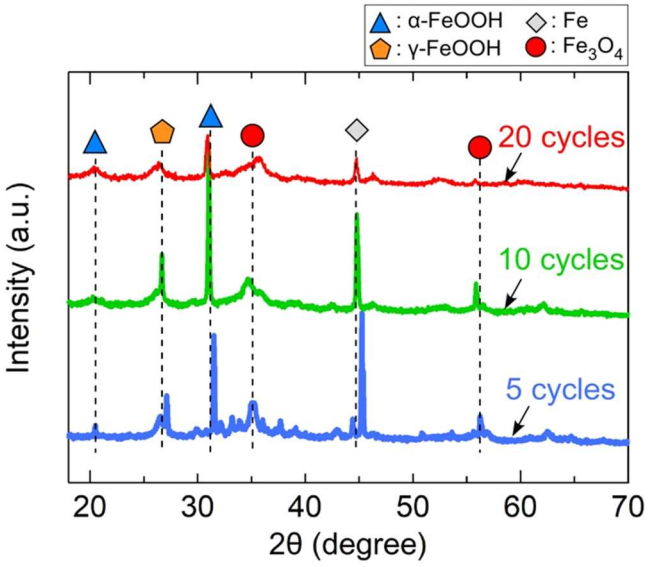


**Figure 4.** XRD patterns of rust layers formed on SM490 specimens after repeating wet/dry cycles.

with rust formation, potentiodynamic polarization measurements were conducted in 1 wt% NaCl solution for the SM490 specimens before and after wet/dry cycling, as shown in Fig. 6.

As discussed in the Introduction, the present study primarily focuses on cathodic polarization behavior. For the specimen without rust (before wet/dry cycles), diffusion-limited oxygen reduction was observed in the potential range from −0.6 to −0.9 V, exhibiting a low current density of approximately $2 \times 10^{-5}$ A cm$^{-2}$. At potentials below −0.9 V, the cathodic current increased logarithmically with decreasing potential, corresponding to hydrogen evolution reaction. These results represent typical cathodic behaviors of carbon steel in NaCl solutions.[41] In contrast, specimens subjected to wet/dry cycling exhibited significantly higher cathodic current densities over the entire cathodic potential region compared with the rust-free specimen. Furthermore, below −0.7 V, the magnitude of cathodic current slightly increased with increasing number of cycles. These results clearly indicate that rust formation and growth promote cathodic reaction.

Although the main focus of this study is cathodic behavior, it is noteworthy that the formation of the rust layer also affected the anodic current in Fig. 6. Compared to the specimen without rust, the anodic current increased after 5 cycles while it decreased at 10 and 20 cycles. Similar phenomena have been reported in previous studies.[27,28] Based on these studies, the increase in anodic current during the initial cycles is attributed to the cracking in the rust layer, which facilitates the transportation of the corrosive electrolytes (such as $Cl^-$) to the steel. In contrast, at later cycles, the formation of a protective inner last layer is considered to suppress the anodic reaction.[27] Although anodic processes are not examined in detail here, the observed trend is consistent with established corrosion behavior of rusted steels.

***Potentiostatic polarization behavior of the rust layer.***—Based on the potentiodynamic polarization results shown in Fig. 6, the presence of rust was found to significantly enhanced cathodic reactions. To further clarify the cathodic processes occurring on rust layers, potentiostatic polarization measurements were conducted at −1.0 V in 1 wt% NaCl solution. A sufficiently negative potential of −1.0 V was selected to minimize the influence of competing anodic reactions.

Figure 7 shows the time variation of the cathodic current during potentiostatic polarization at −1.0 V. For the specimen before wet/

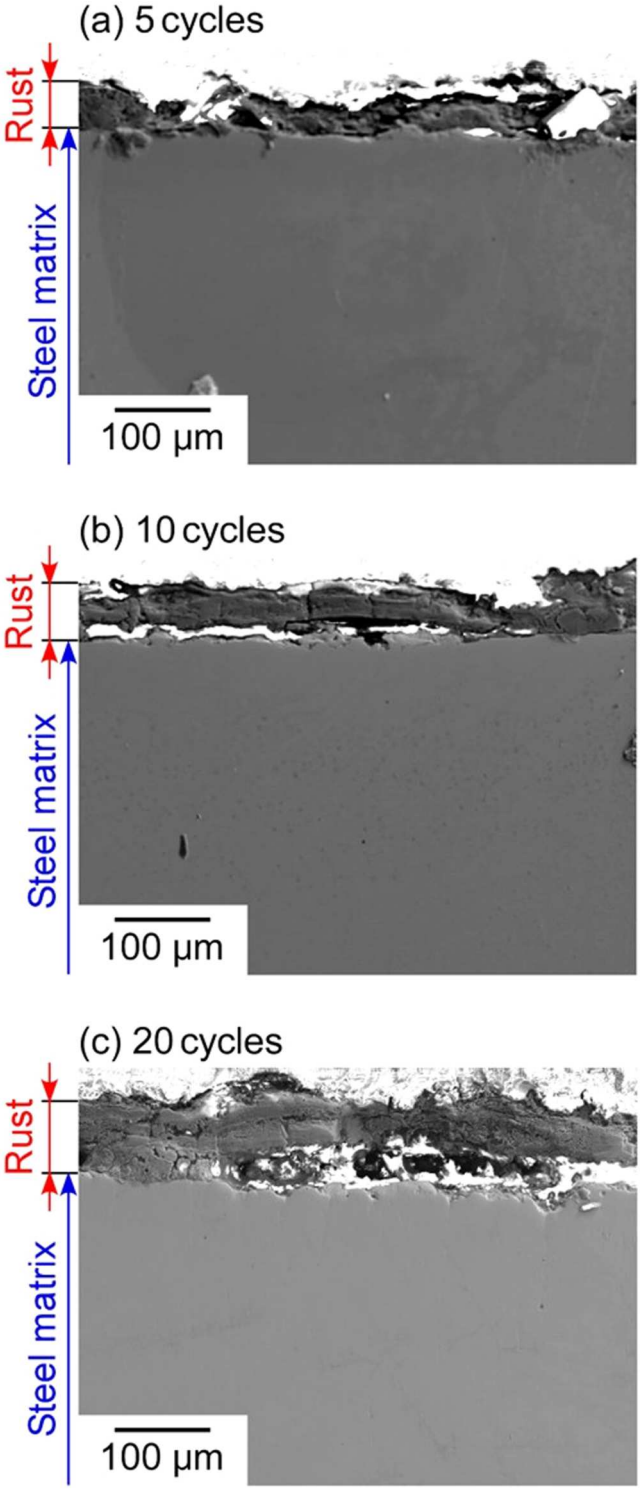


**Figure 5.** Cross-sectional SEM images of rust layers formed on SM490 specimens after repeating wet/dry cycles: (a) after 5 cycles, (b) after 10 cycles, and (c) after 20 cycles.

dry cycling (without rust), the cathodic current remained nearly constant at approximately $3 \times 10^{-5}$ A cm$^{-2}$ throughout the measurement period, with no significant changes observed. Specimens subjected to wet/dry cycling exhibited higher cathodic currents than the specimen without rust, and the current increased with increasing number of cycles. These results demonstrate that rust formation and growth markedly enhances cathodic reaction,

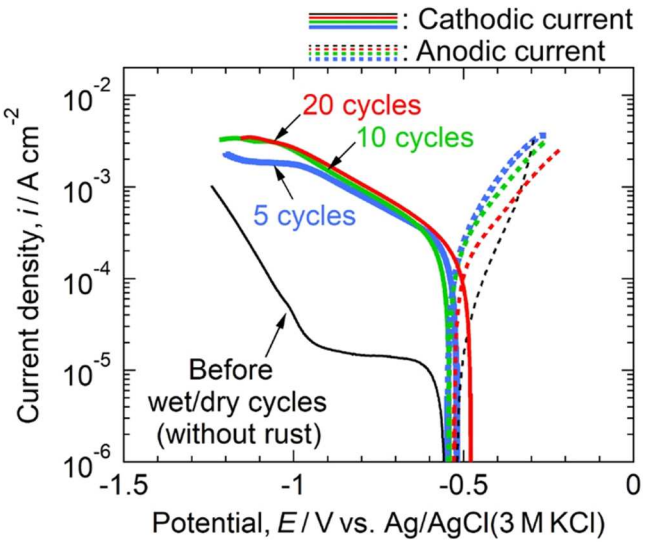


**Figure 6.** Potentiodynamic polarization curves of SM490 specimens with rust (after repeating wet/dry cycles) and without rust in 1 wt% NaCl solution. Solid and dashed lines show the cathodic and anodic polarization curves, respectively.

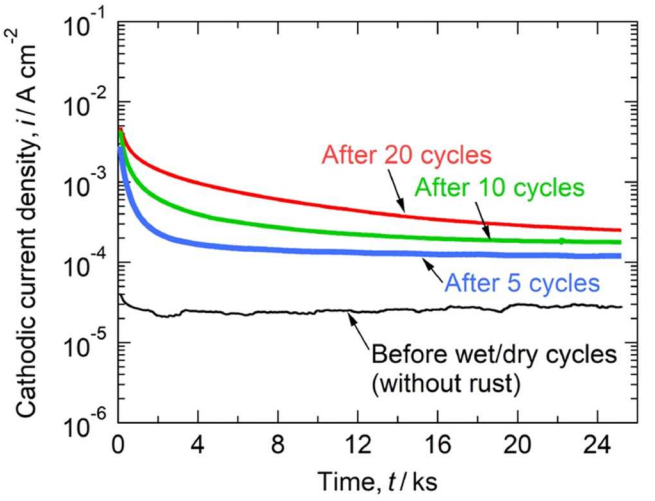


**Figure 7.** Time variation of cathodic current during potentiostatic polarization at −1.0 V for SM490 specimens with rust (after repeating wet/dry cycles) and without rust in 1 wt% NaCl solution.

consistent with the potentiodynamic polarization behavior shown in Fig. 6.

Focusing on time-dependent behavior, rusted specimens after the wet/dry cycles initially exhibited high current values exceeding $1 \times 10^{-3}$ A cm$^{-2}$. The current subsequently decreased and reached to the order of $10^{-4}$ A cm$^{-2}$. After this decline, the current value remained relatively stable and maintained the order of $10^{-4}$ A cm$^{-2}$ until the end of polarization. Specimens subjected to a larger number of wet/dry cycles exhibited slower current decay and higher steady-state current values.

***Reduction reaction of rust components.***—Figure 8 presents optical microscopy images of the specimen surfaces after potentiostatic polarization in Fig. 7. Compared with surfaces prior to polarization (Fig. 3), the rust layers exhibited a distinct color change from reddish to black following polarization. The corresponding XRD patterns of the polarized specimens are shown in Fig. 9.

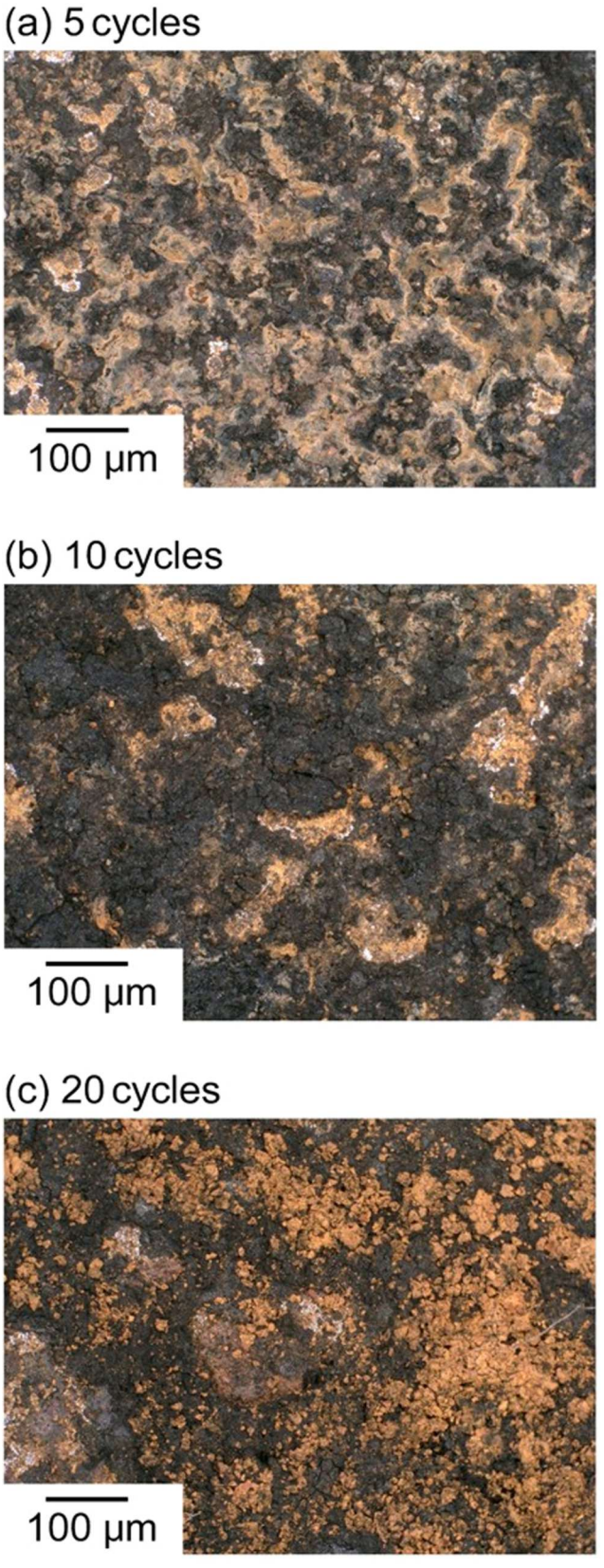


**Figure 8.** Optical microscopy images of rust layers formed on SM490 specimens after repeating wet/dry cycles—(a) after 5 cycles, (b) after 10 cycles, and (c) after 20 cycles— after potentiostatic polarization at −1.0 V as shown in Fig. 7.

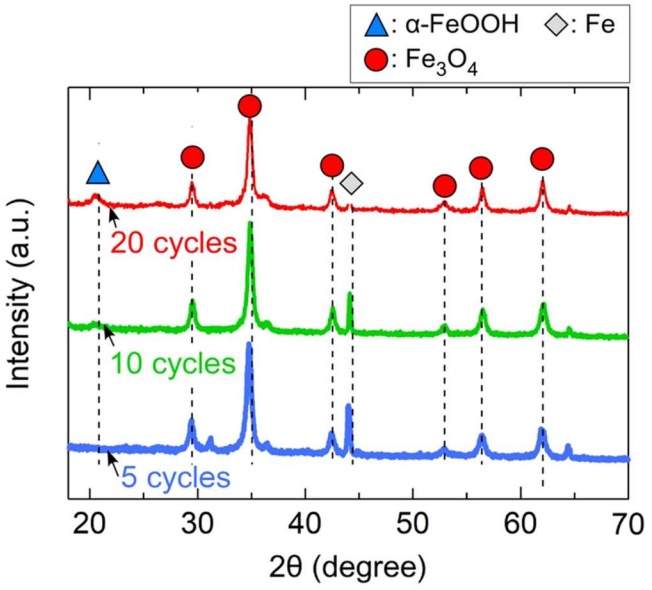


**Figure 9.** XRD patterns of rust layers after potentiostatic polarization at −1.0 V as shown in Fig. 7.

Compared with the data before polarization (Fig. 4), diffraction peaks associated with FeOOH became significantly weaker, whereas peaks corresponding to $Fe_3O_4$ were markedly intensified after polarization. These results indicate a decrease in FeOOH content accompanied by an increase in $Fe_3O_4$ within the rust layer during polarization. Because $Fe_3O_4$ exhibits black coloration, this compositional transformation is consistent with the optical observations in Fig. 8.

FeOOH is known to undergo electrochemical reduction according to the following reaction:[42–45]

$$3FeOOH + H^+ + e^- \rightarrow Fe_3O_4 + 2H_2O \quad [1]$$

Therefore, it is reasonable to conclude that this reduction reaction proceeds during potentiostatic polarization in Fig. 7. The time-dependent decrease in cathodic current observed in Fig. 7 can be attributed to the progressive reduction and consumption of FeOOH within the rust layer. In other words, as the amount of reducible FeOOH decreases with polarization time, the contribution of this reduction reaction diminishes, resulting in the observed decline in cathodic current. Notably, specimens subjected to fewer wet/dry cycles exhibited faster current decay, which is consistent with their smaller amount of rust and correspondingly lower FeOOH content. Figure 10 shows cross-sectional SEM images of the specimens after potentiostatic polarization in Fig. 7. Compared to Fig. 5 (before polarization), the rust layer thickness decreased slightly due to polarization, but the difference was minimal overall.

***Implication of additional cathodic reactions attributed to $Fe_3O_4$.***—As shown in Fig. 7, after the cathodic current decreased and reached steady-state values, specimens with rust layers continued to exhibit higher cathodic currents than the rust-free specimen throughout the polarization period. At this stage, surface observations (Fig. 8) and XRD results (Fig. 9) indicate that the rust layer consisted predominantly of $Fe_3O_4$. Because $Fe_3O_4$ is stable and is not further reduced under this condition,[46] the sustained cathodic current observed at steady state cannot be attributed to continuous reduction of rust components. This finding suggests that in addition to the reduction reaction of rust components, other cathodic reactions occurred on the rust layer.

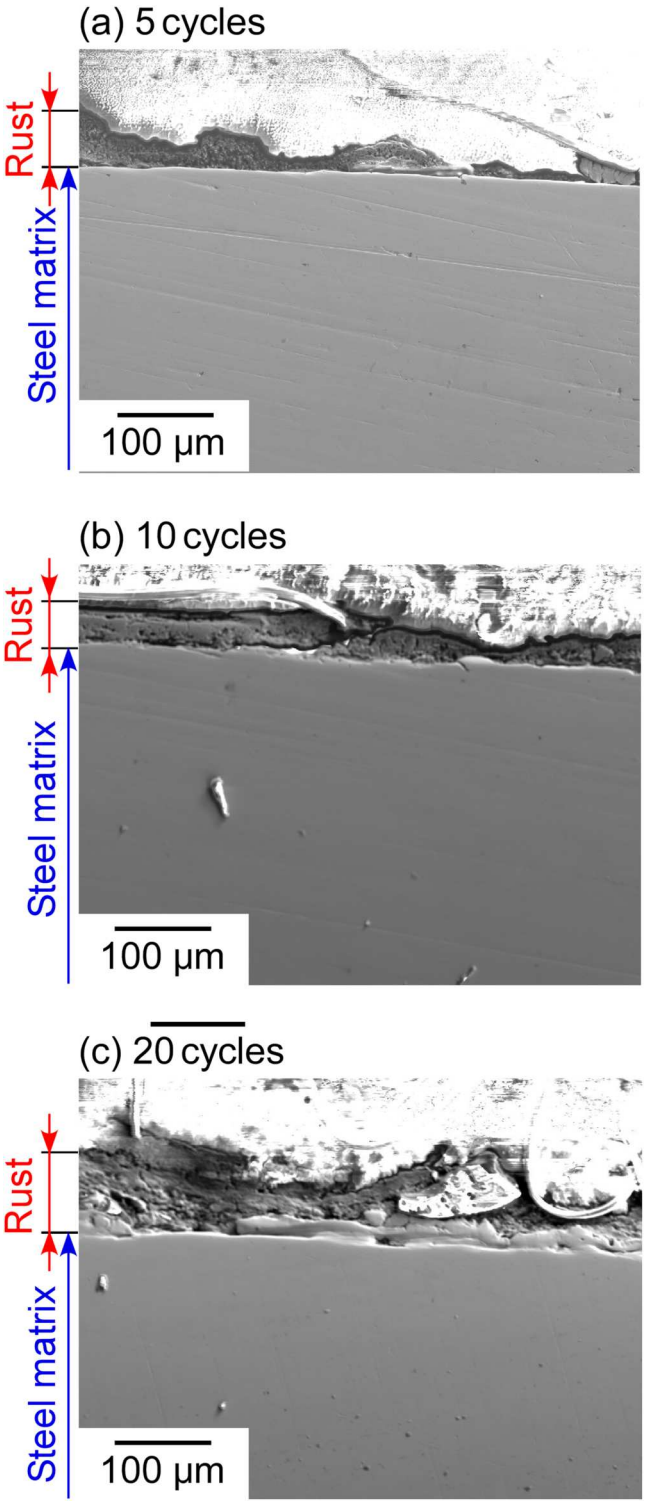


**Figure 10.** Cross-sectional SEM images of rust layers formed on SM490 specimens after repeating wet/dry cycles —(a) after 5 cycles, (b) after 10 cycles, and (c) after 20 cycles— after potentiostatic polarization at −1.0 V as shown in figure 7.

Figure 11 shows the relationship between the steady-state cathodic current (measured at 25 ks in Fig. 7) and the rust layer thickness. The thickness was determined from cross-sectional SEM observations (Fig. 10). In Fig. 10, although the thickness was not uniform across different locations, the measurements at five different points for each specimen were averaged and are plotted in Fig. 11. Since the data for all specimens are aligned almost linearly, a clear

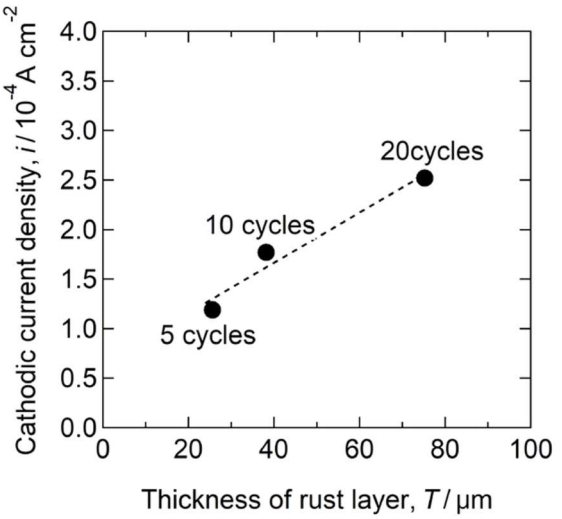


**Figure 11.** Relationship between cathodic current measured at 25 ks of the potentiostatic polarization in Fig. 7 and the average thickness of the rust layer for SM490 specimens subjected to wet/dry cycles.

correlation between steady-state cathodic current and rust layer thickness was observed. Because the rust layer was primarily composed of $Fe_3O_4$ at this time, the thickness of the rust layer can be regarded as the amount of $Fe_3O_4$, or the available $Fe_3O_4$ surface area participating in cathodic reactions. These results therefore indicate that cathodic reactions other than the FeOOH reduction reaction are closely associated with $Fe_3O_4$.

Among possible cathodic reactions on $Fe_3O_4$, the contribution of oxygen reduction is expected to be limited. Oxygen reduction is diffusion-limited, and typically produces maximum cathodic current on the order of $10^{-5}$ A cm$^{-2}$,[41] which are significantly lower than the steady-state cathodic currents observed in Fig. 7. Furthermore, $Fe_3O_4$ is a stable compound and is not further reduced.[46] The electrolyte was NaCl and contained no additional reducible species. Accordingly, the dominant cathodic reaction occurring on $Fe_3O_4$ is reasonably attributed to the hydrogen evolution reaction.

$Fe_3O_4$ has been reported as an electrocatalytically active material for hydrogen evolution reaction in energy-conversion systems such as water electrolysis and fuel cells owing to its spinel structure and favorable electronic conductivity.[47,48] Although most previous studies have been conducted under strongly alkaline and elevated-temperature conditions, to the best of our knowledge, there is no information regarding the hydrogen evolution reactivity of $Fe_3O_4$ under neutral or acidic pH and room temperature, which are conditions similar to the atmospheric corrosion environment assumed in this study. On the other hand, the results obtained in this paper suggest that the hydrogen evolution reaction can actively proceed on $Fe_3O_4$ even under such conditions.

***Preparation of $Fe_3O_4$ sintered specimens.***—As discussed above, in addition to the reduction of rust components, other cathodic reactions occur on the rust layer, and these reactions are likely to be predominantly associated with $Fe_3O_4$. However, the electrochemical behavior of rust layers formed during wet/dry cycling reflects the combined response of multiple phases, including $Fe_3O_4$ and FeOOH. Consequently, direct evaluation of the intrinsic electrochemical contribution of $Fe_3O_4$ from rusted specimen alone is difficult. Therefore, to isolate the electrochemical contribution of $Fe_3O_4$, a $Fe_3O_4$-dominant specimen was fabricated by spark plasma sintering of commercial $Fe_3O_4$ powder. The detailed sintering conditions were described earlier in Experimental Methods section.

Optical microscopy images of the sintered $Fe_3O_4$ specimen are shown in Figs. 12a and 12b. The surface exhibited no visible cracks or pores, indicating that the sintered specimen possessed high density and structural integrity. The corresponding surface hight profile

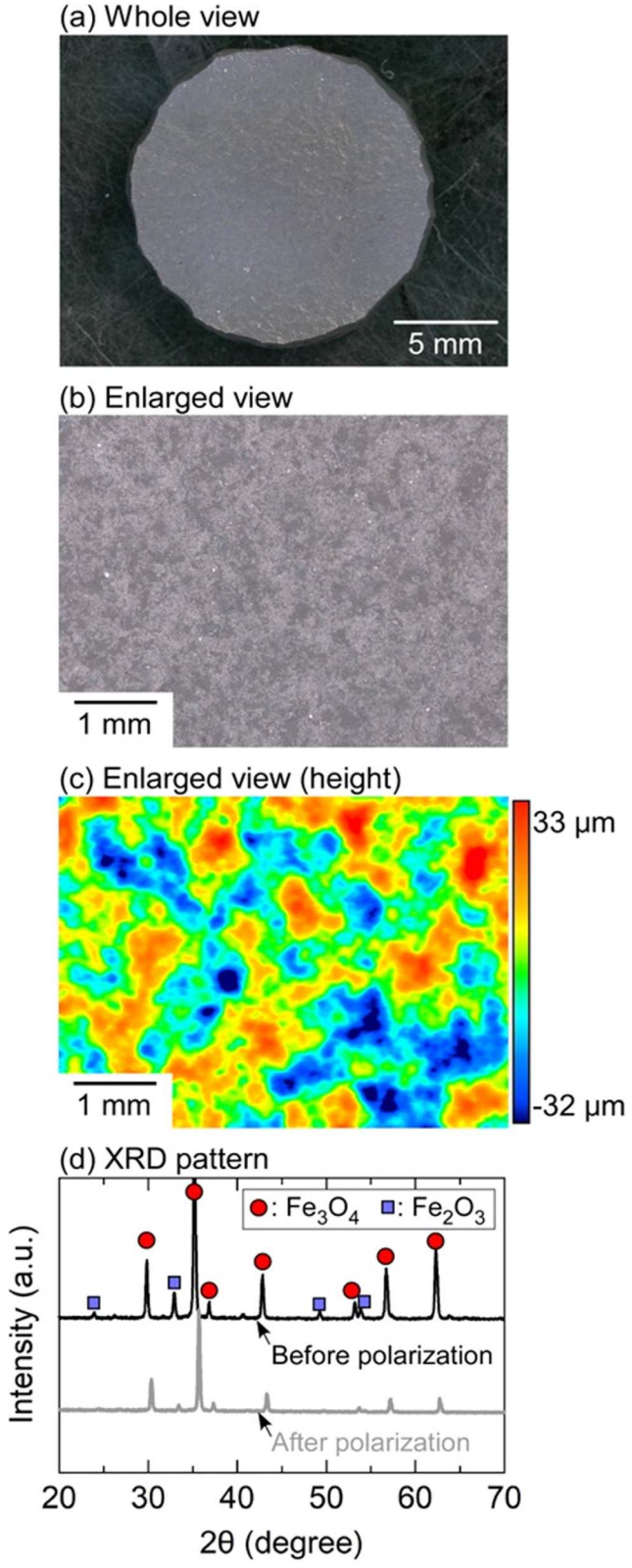


**Figure 12.** (a)–(b) Optical microscopy image, (c) topographic height profile, and (d) XRD pattern of the $Fe_3O_4$ sintered specimen.

Fig. 12c confirms that the specimen surface was nearly flat, with only minor surface roughness of approximately 60 μm.

The XRD pattern shown in Fig. 12d (black graph, labeled "before polarization") confirms that $Fe_3O_4$ is the dominant phase in the specimen. Minor diffraction peaks corresponding to $Fe_2O_3$ were also detected, which are attributed to impurities originating from the starting powder (explained in Experimental Methods "Preparation of $Fe_3O_4$ sintered specimen" section). The intensity of the main peak of $Fe_3O_4$ ($2\theta = 35°$) is approximately 8.6 times greater than that of $Fe_2O_3$ ($2\theta = 33°$). Although this is only a rough estimation since no Rietveld refinement or similar analysis was conducted, it is reasonable to consider that $Fe_3O_4$ is the dominant component.

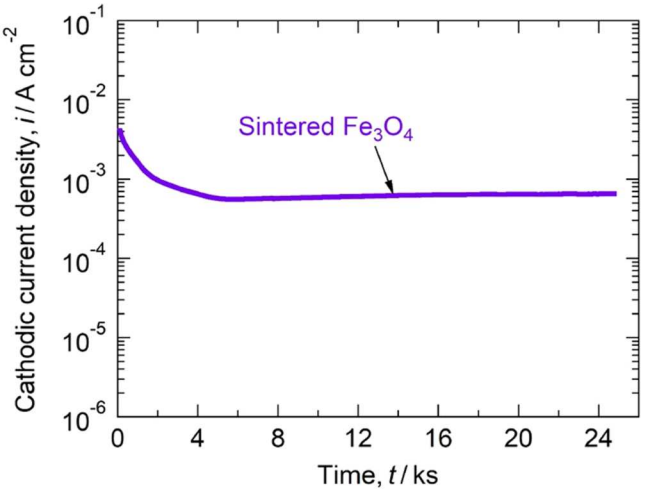


**Figure 13.** Time variation of cathodic current during potentiostatic polarization at −1.0 V for the $Fe_3O_4$ specimen in 1 wt% NaCl solution.

***Cathodic polarization behavior of sintered $Fe_3O_4$ specimen.—*** Potentiostatic polarization measurements were performed on the sintered $Fe_3O_4$ specimen in 1 wt% NaCl solution at −1.0 V under conditions identical to those used for the rusted SM490 specimens shown in Fig. 7. The time-dependent variation of cathodic current during polarization is shown in Fig. 13. The $Fe_3O_4$ specimen initially exhibited a high cathodic current of approximately $4 \times 10^{-3}$ A cm$^{-2}$, followed by a rapid decrease within approximately 2 ks before reaching a steady-state value. As indicated by the XRD results in Fig. 12d, the sintered specimen contained a minor amount of $Fe_2O_3$ impurity. The high current observed during the initial stage is therefore attributed to reduction of $Fe_2O_3$ to $Fe_3O_4$. As this reduction proceeds and $Fe_2O_3$ is consumed, its contribution to the cathodic current diminishes, resulting in the observed current decline. The XRD results of the $Fe_3O_4$ specimen after the polarization is also shown in Fig. 12d. The characteristic peaks of $Fe_3O_4$ are clearly observed both before and after polarization, indicating that $Fe_3O_4$ does not transform into other phases during the polarization. On the other hand, the peaks assigned to $Fe_2O_3$ are much less prominent after the polarization. Although a small $Fe_2O_3$ peak at $2\theta = 33°$ is still observed, the signals at $2\theta = 24°$, 49° and 54° are nearly flat and the corresponding $Fe_2O_3$ peaks have almost completely disappeared after the polarizaton. These results also supprots our interpretation that the intial high current observed in Fig. 13 was cuased by the reduction of $Fe_2O_3$.

Importantly, after reaching steady-value, the cathodic current for the sintered $Fe_3O_4$ specimen remained within the same order of magnitude ($10^{-4}$ to $10^{-3}$ A cm$^{-2}$) as that observed for rusted SM490 specimens in Fig. 7. Since the rusted specimens in Fig. 7 were composed of multiple phases (FeOOH and $Fe_3O_4$), it was not possible to conclusively attribute the steady-state cathodic current sorely to $Fe_3O_4$. However, the fact that the sintered $Fe_3O_4$ specimen, which is predominantly composed of $Fe_3O_4$, exhibited a comparable steady-state current clearly indicates that $Fe_3O_4$ itself functions as a major active site for cathodic reactions at this time.

***Discussion on the effect of $Fe_3O_4$ content on hydrogen evolution and permeation.—***Based on the results presented so far, it is suggested that cathodic reactions occur actively on $Fe_3O_4$. As

discussed earlier, the dominant cathodic reaction occurring on $Fe_3O_4$ is considered to be the hydrogen evolution reaction. In contrast, based on the literature, FeOOH exhibits relatively low electronic conductivity because of its crystal structure, and cannot adequately supply electrons required for electron transfer reactions (hydrogen evolution reaction).[49] In addition, unlike FeOOH, which consists exclusively of trivalent iron ($Fe^{3+}$), $Fe_3O_4$ contains $Fe^{2+}$ states that are considered to enhance the catalytic activity of the surface for cathodic reactions.[50,51]

Based on these considerations, it is reasonable to expect that an increase in the fraction of $Fe_3O_4$ within the rust layer (i.e., a decrease in the proportion of FeOOH) would enhance hydrogen evolution reactivity. Here, it should be noted that this estimated relationship is not necessarily strictly proportional. This is because various factors, such as the distribution of phases, interface effects between $Fe_3O_4$ and FeOOH, and the surface morphology of the rust layer, can influence electron transport and reaction pathways. On the other hand, as a general trend, it is reasonable to assume that a higher fraction of $Fe_3O_4$ tends to increase hydrogen evolution reactivity. Previous studies have shown that the more actively hydrogen evolution occurs, the more hydrogen permeation into steel is promoted.[23] Therefore, it is estimated that increasing the $Fe_3O_4$ fraction in the rust layer enhances hydrogen permeation into the steel. To verify this interpretation, hydrogen permeation tests were conducted using two rusted SM490 specimens possessing different rust compositions, as described below.

***Influence of $Fe_3O_4$ in rust layers on hydrogen permeation behavior.***—To evaluate the influence of rust composition on hydrogen permeation behavior, hydrogen permeation tests were conducted using two SM490 specimens possessing FeOOH-dominant and $Fe_3O_4$-dominant rust layers. Optical microscopy images of both specimen surfaces are shown in Fig. 14. First, two SM490 specimens were subjected to repeated 10 wet/dry cycles with 1 wt% NaCl droplets, to form FeOOH-dominant rust layers as shown in Fig. 14a. Subsequently, to increase the $Fe_3O_4$ fraction, one specimen was subjected to additional potentiostatic polarization at −1.0 V for 2.5 h in 1 wt% NaCl solution. As shown in Fig. 14b, the surface of this specimen was black, indicating the formation of $Fe_3O_4$-dominant rust. After these processes, the specimens were stored in air at room temperature for more than 24 h prior to the hydrogen permeation tests. This exposure period allowed any hydrogen that may have permeated the steel during above rust formation processes to diffuse out; therefore, it did not affect the results of the hydrogen permeation tests.

The conditions of hydrogen permeation tests were explained earlier in Experimental Methods section. Briefly, the hydrogen detection side (Ni-plated surface without rust) was potentiostatically polarized at 0.14 V in 0.1 M NaOH. After the background current stabilized below 0.07 $\mu A\ cm^{-2}$, 1 wt% NaCl solution (pH 3) was introduced to the cathodic polarization side (rusted surface) and the specimen was polarized at –1.0 V. The time variations of the current on the cathodic polarization side and hydrogen detection side are shown in Figs. 15a and 15b, respectively. In these graphs, cathodic polarization at –1.0 V was started at 1.5 ks, as indicated by dashed lines.

In the case of cathodic polarization side (Fig. 15a), for both specimens, the cathodic current initially exhibits values on the order of $10^{-3}\ A\ cm^{-2}$, and subsequently decreased toward approximately $10^{-4}\ A\ cm^{-2}$. As discussed in Figs. 7–9, this initial high current is considered to be due to the reduction of FeOOH within the rust layer. As FeOOH was reduced and consumed, the cathodic current associated with the reduction of FeOOH decreased. The $Fe_3O_4$-dominant specimen exhibited a more rapid current decrease, which is reasonable because of its lower FeOOH content. For the $Fe_3O_4$-dominant specimen, the cathodic current reached a steady value of approximately $2 \times 10^{-4}\ A\ cm^{-2}$ around 4 ks. This steady value, observed after the reduction of FeOOH had sufficiently proceeded, was considered to result from the hydrogen evolution reaction on $Fe_3O_4$.

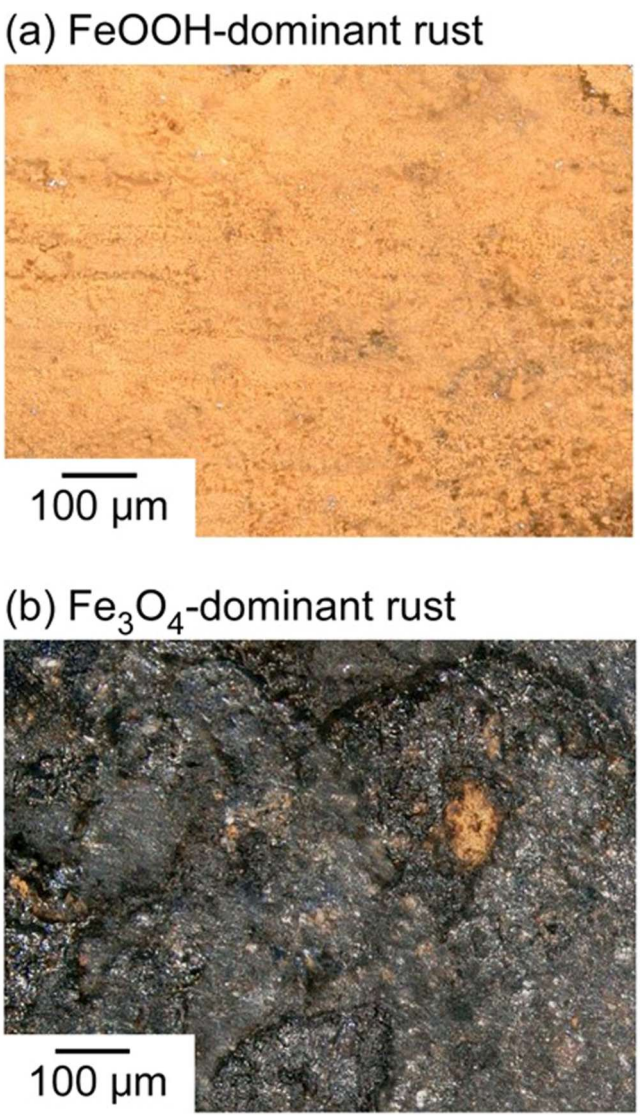


**Figure 14.** Optical microscopy images of rusted surfaces of SM490 specimens used for the hydrogen permeation test: specimens with (a) FeOOH-dominant and (b) $Fe_3O_4$-dominant rust layers.

In the case of hydrogen detection side (Fig. 15b), the anodic current began to increase at 3 ks (that is, approximately 1.5 ks after cathodic polarization was started). This increase indicates that the hydrogen generated on the cathodic polarization side permeated through the specimen and detected on the detection side. It is important that the $Fe_3O_4$-dominant specimen exhibited a higher rate of current increase than the FeOOH-dominant specimen. These results clearly demonstrate that the composition of the rust layer influences hydrogen permeation behavior, and $Fe_3O_4$ enhanced the hydrogen permeation. As discussed in the previous section, $Fe_3O_4$ exhibits higher hydrogen evolution activity than FeOOH, which is considered to be a factor for the enhanced hydrogen permeation observed for the $Fe_3O_4$-dominant specimen.

For both specimens, the detection side current reached similar values beyond approximately 8 ks. This convergence can be reasonably explained by progressive reduction of FeOOH during potentiostatic polarization at –1.0 V in the FeOOH-dominant specimen. In other words, the specimen that was initially FeOOH-dominant ultimately became $Fe_3O_4$-dominant during the measurement, resulting in hydrogen permeation behavior comparable to that of the specimen that was initially $Fe_3O_4$-dominant.

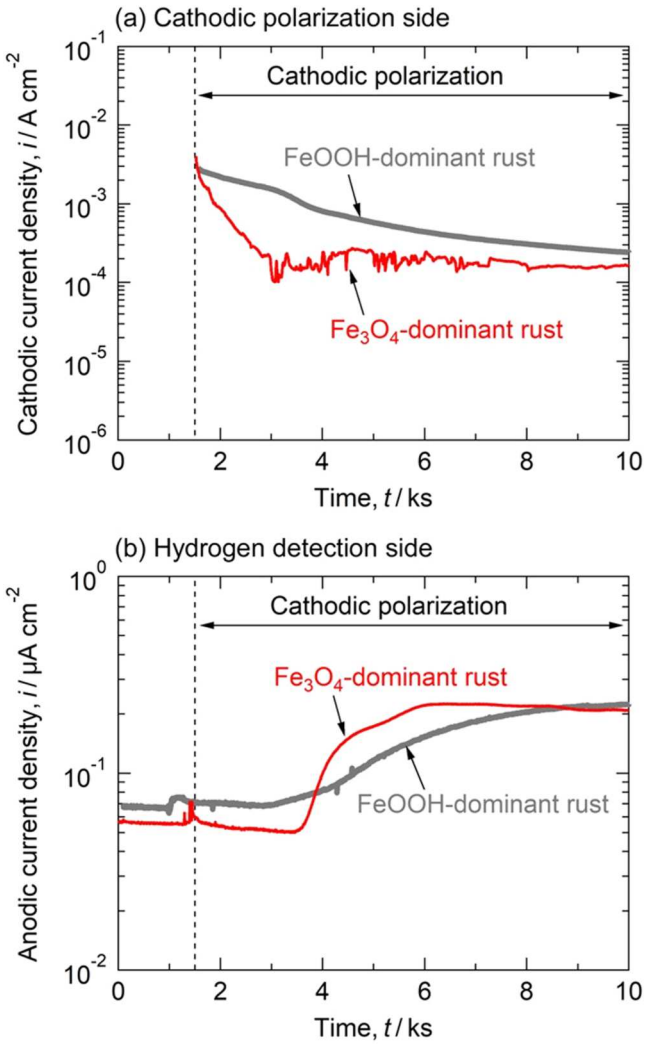


**Figure 15.** Time variation of the measured current during the hydrogen permeation test for SM490 specimens with different $Fe_3O_4$ fractions in the rust layer: (a) cathodic current on the cathodic polarization side, and (b) anodic current on the hydrogen detection side.

Here, it should be noted that the unstable behavior observed in the cathodic current and hydrogen permeation current in Fig. 15 has also been reported in previous studies, and is generally characteristic of rusted specimens.[39,52] This tendency arises because rust layers are composed of multiple phases, such as $Fe_3O_4$ and FeOOH, and reduction reactions (e.g., FeOOH to $Fe_3O_4$) do not proceed uniformly across the surface, resulting in local and stepwise changes in the rust structure that manifest as fluctuations in the current.

Overall, these results demonstrate that rust layer composition significantly influences the cathodic reaction and hydrogen permeation behavior of SM490 carbon steel. In particular, it was found that the $Fe_3O_4$ within the rust layer promotes hydrogen evolution reaction and consequently enhances hydrogen permeation. In actual atmospheric environments, the rust composition varies depending on the steel types, and some practical steels (including weathering steels) develop rust layers with a uniquely high FeOOH content (i.e. low $Fe_3O_4$ fraction). According to the findings of this study, such steels may exhibit greater resistance to hydrogen permeation and embrittlement compared to conventional steels. Further investigation from this perspective will be important for enhancing the service reliability of steel in practical applications. While this study focused on the effect of the rust composition on the hydrogen evolution reaction, it should be noted that other processes, such as hydrogen adsorption, diffusion, and trapping, also play a role in hydrogen embrittlement. Therefore, further investigations targeting these additional processes are necessary to achieve a deeper understanding of hydrogen embrittlement mechanisms.

## Conclusions

1. Rust layers formed on SM490 carbon steel was composed of FeOOH ($\alpha$ and $\gamma$) and $Fe_3O_4$. Potentiodynamic polarization measurements revealed that rust formation and growth significantly enhanced the cathodic reactions.
2. Potentiostatic polarization revealed that the reduction reaction of FeOOH within the rust layer is one of the primary factors contributing to the enhanced cathodic reaction.
3. Even after the reduction reaction of FeOOH proceeded sufficiently, the cathodic current remained high for the rusted SM490 speicmen, indicating that further cathodic reactions occur specifically on the rust layer. It was indicated that the hydrogen evolution reaction can actively proceed on $Fe_3O_4$.
4. Electrochemical hydrogen permeation tests confirmed that rust layer composition influences hydrogen permeation behavior. The specimen possessing $Fe_3O_4$-dominant rust exhibited enhanced hydrogen permeation compared with FeOOH-dominant rust. The higher hydrogen evolution activity on $Fe_3O_4$ is considered to be a key factor responsible for this behavior.

## Acknowledgments

This study was supported by the 32nd ISIJ Research Promotion Grant (Ishihara/Asada Grant) from the Iron and Steel Institute of Japan, and JSPS KAKENHI Grant Numbers JP22K14516.

## ORCID

Mariko Kadowaki https://orcid.org/0000-0002-8988-3545
Masahiro Yamamoto https://orcid.org/0009-0002-1861-7757
Hideki Katayama https://orcid.org/0000-0001-7947-4687
Arkapol Saengdeejing https://orcid.org/0000-0001-8739-3262
Taichi Abe https://orcid.org/0000-0002-5065-0939
Ryoji Sahara https://orcid.org/0000-0003-0788-2985
Kotaro Doi https://orcid.org/0000-0002-5204-1088
Yoshiharu Murase https://orcid.org/0000-0001-7390-851X
Sachiko Hiromoto https://orcid.org/0000-0003-4666-6708
Yusuke Tsutsumi https://orcid.org/0000-0002-9483-1256

## References

1. L. Liu, L. Chen, and R. Case, *J. Electrochem. Soc.*, **169**, 112697 (2022).
2. T. Rubben, K. Baert, T. Depover, K. Verbeken, R. I. Revilla, and I. D. Graeve, *J. Electrochem. Soc.*, **169**, 111503 (2022).
3. S. J. Kim, *J. Electrochem. Soc.*, **171**, 061501 (2024).
4. T. Zakroczymski and Z. Szklarska-Smialowska, *J. Electrochem. Soc.*, **132**, 2548 (1985).
5. T. Tsuru, Y. Huang, M. R. Ali, and A. Nishikata, *Corros. Sci.*, **47**, 2431 (2005).
6. Y. Huang and Y. Zhu, *Corros. Sci.*, **47**, 1545 (2005).
7. E. Akiyama, S. Li, T. Shinohara, Z. Zhang, and K. Tsuzaki, *Electrochim. Acta*, **56**, 1799 (2011).
8. S. Ajito, E. Tada, A. Ooi, and A. Nishikata, *ISIJ Int.*, **59**, 1659 (2019).
9. P. Li, J. Wang, M. Du, and L. Qiao, *Int. J. Hydro. Ene*, **48**, 35862 (2023).
10. H. Kakinuma, S. Hiromoto, T. Hojo, S. Ajito, M. Koyama, and E. Akiyama, *Corros. Sci.*, **232**, 112043 (2024).
11. G. Sudha, M. Rohwerder, and D. Vijayshankar, *Corros. Sci.*, **259**, 113449 (2026).
12. M. Morcillo, B. Chico, J. Alcántara, I. Díaz, R. Wolthuis, and D. de la Fuente, *J. Electrochem. Soc.*, **163**, C426 (2016).
13. D. A. Koleva, J. H. W. de Wit, K. van Breugel, Z. F. Lodhi, and G. Ye, *J. Electrochem. Soc.*, **154**, C261 (2007).
14. M. Morcillo, B. Chico, D. de la Fuente, J. Alcántara, I. O. Wallinder, and C. Leygraf, *J. Electrochem. Soc.*, **164**, C8 (2016).
15. I. Suzuki, Y. Hisamatsu, and N. Masuko, *J. Electrochem. Soc.*, **127**, 2210 (1980).
16. J. T. Keiser, C. W. Brown, and R. H. Heidersbach, *J. Electrochem. Soc.*, **129**, 2686 (1982).
17. T. E. Graedel and R. P. Frankenthal, *J. Electrochem. Soc.*, **137**, 2385 (1990).
18. S. Li and L. H. Hihara, *J. Electrochem. Soc.*, **159**, C147 (2012).
19. B. Wang, Y. Zhao, X. Cheng, X. Zhang, L. Wang, Z. Li, C. Liu, D. Zhang, and X. Li, *Corros. Sci.*, **255**, 113117 (2025).
20. X. Han and M. Sakairi, *Corros. Sci.*, **231**, 111993 (2024).
21. K. Gong, M. Wu, and G. Liu, *Corros. Sci.*, **165**, 108382 (2020).

22. H. Tian, X. Wang, Z. Cui, Q. Lu, L. Wang, L. Lei, Y. Li, and D. Zhang, *Corros. Sci.*, **144**, 145 (2018).
23. M. Nagumo, H. Uyama, and M. Yoshizawa, *Corros. Sci.*, **44**, 947 (2001).
24. T. Nishimura, H. Katayama, K. Noda, and T. Kodama, *Corros. Sci.*, **42**, 1611 (2000).
25. K. Asami and M. Kikuchi, *Corros. Sci.*, **45**, 2671 (2003).
26. Q. X. Li, Z. Y. Wang, W. Han, and E. H. Han, *Corros. Sci.*, **50**, 365 (2008).
27. L. Hao, S. Zhang, J. Dong, and W. Ke, *Corros. Sci.*, **58**, 175 (2012).
28. W. Chen, L. Hao, J. Dong, and W. Ke, *Corros. Sci.*, **83**, 155 (2014).
29. K. Otani, T. Tsukada, and F. Ueno, *Mater. Trans.*, **62**, 763 (2021).
30. C. Hayama, M. Kadowaki, Y. Murase, H. Katayama, T. Hara, Y. Hara, H. Watanabe, I. Shitanda, and M. Itagaki, *ISIJ Int.*, **64**, 1820 (2024).
31. M. Kadowaki, H. Katayama, and M. Yamamoto, *Corros. Sci.*, **218**, 111190 (2023).
32. Inorganic Material Database (Atom Work), National Institute for Materials Science, https://crystdb.nims.go.jp/crystdb/search-phase-details?condition_value=Fe+O&pageDetails=1&page=1&history=true&phase_diagram_id=4295868358 (accessed 21 January 2026).
33. B. Sundman, *J. Phase Equilib.*, **12**, 127 (1991).
34. M. Kadowaki, H. Katayama, and M. Yamamoto, *Corros. Sci.*, **211**, 110918 (2023).
35. M. Kadowaki and H. Katayama, *Corros. Sci.*, **222**, 111379 (2023).
36. M. Kadowaki, T. Moronaga, A. Nakamura, Y. Murase, T. Hashimoto, H. Katayama, K. Takanabe, and Y. Tsutsumi, *J. Phys. Chem. C*, **129**, 15939 (2025).
37. M. A. V. Devanathan and Z. Stachurski, *Proc. A*, **270**, 90 (1962).
38. M. A. V. Devanathan, Z. Stachurski, and W. Becki, *J. Electrochem. Soc.*, **110**, 886 (1963).
39. S. Li, E. Akiyama, T. Shinohara, K. Matsuoka, and W. Oshikawa, *ISIJ Int.*, **53**, 1062 (2013).
40. J. Peng, V. Ji, and W. Seiler, *Mater. Sci. Forum*, **490-491**, 153 (2005).
41. M. Kadowaki, H. Katayama, and M. Yamamoto, *ISIJ Int.*, (In press).
42. A. Kuch, *Corros. Sci.*, **28**, 221 (1988).
43. M. Morcillo, I. Díaz, B. Chico, H. Cano, and D. de la Fuente, *Corros. Sci.*, **83**, 6 (2014).
44. X.-L. Gao, Y. Han, G.-Q. Fu, M.-Y. Zhu, and X.-Z. Zhang, *Acta Metall. Sin.*, **29**, 1025 (2016).
45. F. Wu, Z. Hu, X. Liu, C. Su, and L. Hao, *Corros. Sci.*, **315**, 131968 (2022).
46. T. Misawa, K. Hashimoto, and S. Shimodaira, *Corros. Sci.*, **14**, 131 (1974).
47. J. Zhang, X. Shang, H. Ren, J. Chi, H. Fu, B. Dong, C. Liu, and Y. Chai, *Adv. Mater.*, **31**, 1905107 (2019).
48. J. Xiang et al., *J. Alloys Compd.*, **1036**, 181652 (2025).
49. M. Stratmann and J. Müller, *Corros. Sci.*, **36**, 327 (1994).
50. E. R. Vago, E. J. Calvo, and M. Stratmann, *Electrochim. Acta*, **39**, 1655 (1994).
51. R. Krieg, M. Rohwerder, S. Evers, B. Schuhmacher, and J. Schauer-Pass, *Corros. Sci.*, **65**, 119 (2012).
52. S. Ajito, E. Tada, A. Ooi, and A. Nishikata, *ISIJ Int.*, **61**, 1186 (2021).